



Contents lists available at ScienceDirect

# International Journal of Rock Mechanics & Mining Sciences

journal homepage: [www.elsevier.com/locate/ijrmms](http://www.elsevier.com/locate/ijrmms)

## The distinct element analysis for hydraulic fracturing in hard rock considering fluid viscosity and particle size distribution

Hiroyuki Shimizu<sup>a,\*</sup>, Sumihiko Murata<sup>b</sup>, Tsuyoshi Ishida<sup>b</sup><sup>a</sup> Department of Civil and Earth Resources Engineering, Kyoto University, Katsura, Nishikyo-ku, Kyoto 615-8540, Japan<sup>b</sup> Department of Civil and Earth Resources Engineering, Kyoto University, Japan

### ARTICLE INFO

#### Article history:

Received 15 March 2010

Received in revised form

24 November 2010

Accepted 13 April 2011

Available online 10 May 2011

#### Keywords:

Distinct element method (DEM)

Hydraulic fracturing

Rock

Acoustic emission (AE)

Viscosity

Particle size distribution

### ABSTRACT

A series of simulations for hydraulic fracturing in competent rock was performed by using the flow-coupled DEM code to discuss the influence of the fluid viscosity and the particle size distribution. The simulation results show good agreement with experimental results that contain the AE measurement data. The following observations can be made. When a low viscosity fluid is used, the fluid infiltrates into the fracture immediately. On the other hand, when a high viscosity fluid is used, the fluid infiltrates slowly into the crack after the fracture first elongates. Although tensile cracks are dominantly generated in the simulation, the energy released from a tensile crack becomes small because the tensile strength of rock is obviously small compared with the compressive strength. Such a small AE is easily buried in a noise and difficult to be measured in an experiment. Therefore, in AE measurement experiment, shear type AE with large energy is dominantly observed, as many previous researches have indicated.

© 2011 Elsevier Ltd. All rights reserved.

### 1. Introduction

To better understand the mechanics of hydraulic fracturing, a considerable amount of research has been carried out in the past few decades. According to the conventional theory, hydraulic fracturing is formed by tensile crack generation [1]. On the other hand, the shear type mechanisms was observed in most of the acoustic emission (AE) events recorded during the laboratory and field hydraulic fracturing experiments [2–5]. Ishida et al. [6] carried out a laboratory hydraulic fracturing experiments using low viscosity water and higher viscosity oil. The source mechanisms of AE events indicates that shear type mechanisms are dominant when low viscosity fluid is injected, and both shear and tensile type mechanisms are observed when high viscosity fluid is injected.

In addition, Matsunaga et al. [7] conducted hydraulic fracturing experiments for various rocks and acrylic resin, and found that rock texture, such as grain size, affects the hydraulic fracturing mechanism. Ishida et al. [6] extended this work and the hydraulic fracturing experiments were conducted for four different types of granitic rock specimens with different grain size in order to investigate the influence of grain size on induced crack geometry and fracturing mechanism [8–10]. The fault plane solutions of AE indicated that the dominant micro-fracturing mechanism becomes tensile rather than shear with decreasing grain size. Their experimental results indicate that texture of rock like grain size of granitic rocks considerably

affects the geometry, surface roughness and microcracking mechanism of hydraulically induced cracks.

To give a rational explanation for such disagreement between conventional theory and AE monitoring, and to better understand the hydraulic fracturing mechanism, various numerical analysis techniques have been developed. The Finite Element Method (FEM) and the Boundary Element Method (BEM) have been commonly used to simulate hydraulic fracturing in complex three-dimensional structures [11,12]. Al-Busaidi et al. [13] simulated hydraulic fracturing in granite by using the distinct element method (DEM), and the results were compared with the AE data from the experiment. However, the simulation results showed that the disagreement mentioned above was not solved successfully. Therefore, the mechanism of hydraulic fracture propagation has not been sufficiently clarified.

In this paper, a fluid flow algorithm that can consider the fluid viscosity and permeability is introduced into the DEM program to reproduce the hydraulic fracturing. A series of simulations for hydraulic fracturing in hard rock was performed by using the flow-coupled DEM code to discuss the influence of the fluid viscosity and the particle size distribution, and to obtain insights that gave the rational explanation to the disagreement between conventional theory and the AE monitoring results.

### 2. Simulation methodology

#### 2.1. Formulation of mechanics of bonded particles

The DEM for granular materials was originally developed by Cundall and Strack [14]. They developed a well-known commercially

\* Corresponding author. Present address: Large-Scale Environmental Fluid Dynamics Laboratory, Institute of Fluid Science, Tohoku University, 2-1-1 Katahira Aoba-ku Sendai, 980-8577, Japan. Tel./fax: +81 22 217 5235.

E-mail address: [shimizu82@gmail.com](mailto:shimizu82@gmail.com) (H. Shimizu).

available DEM code (particle flow code (PFC)) [15]. In this study, two-dimensional distinct element method (2D DEM) was employed, and we have written our own DEM code to study hydraulic fracturing. Since thorough details of fundamental DEM algorithm can be found in [14,15], only a summary of the primary differences between the DEM code used in this research and the parallel-bond model in the PFC<sup>2D</sup> code [15] will be given.

Although the DEM is one of the numerical techniques based on the discontinuum model, it can be applied also to the continuum by introducing bonds between particles. In two dimensional DEM, the intact rock is modeled as a dense packing of small rigid circular particles. Neighboring particles are bonded together at their contact points with normal, shear, and rotational springs and interact with each other.

The increments of normal force  $f_n$ , the tangential force  $f_s$ , and the moment  $f_\theta$  can be calculated from the relative motion of the bonded particles, and are given as

$$f_n = k_n(dn_j - dn_i) \tag{1}$$

$$f_s = k_s \left[ ds_j - ds_i - \frac{L}{2}(d\theta_j + d\theta_i) \right] \tag{2}$$

$$f_\theta = k_\theta(d\theta_j - d\theta_i) \tag{3}$$

where  $k_n$ ,  $k_s$ , and  $k_\theta$  are the stiffnesses of normal, shear, and rotational springs, respectively;  $dn$ ,  $ds$ , and  $d\theta$  are normal and shear displacements and rotation of particles;  $r_i$  and  $r_j$  are the radii of the bonded particles. A bond between the particles is presented schematically as a gray rectangle in Fig. 1, where  $L$  and  $D$  are the bond length and the bond diameter, respectively.  $D$  is obtained from harmonic mean of the radius of two particles.  $L$  and  $D$  are given by

$$L = r_i + r_j \tag{4}$$

$$D = \frac{4r_i r_j}{r_i + r_j} \tag{5}$$

Since the DEM is formulated as a fully dynamic system, small amounts of viscous damping are necessary to provide dissipation of high-frequency vibration. If contact damping is not introduced, the assemblies will not be able to reach equilibrium. Contact damping operates on the relative velocities at the contacts and is represented by dashpots acting in the normal and shear directions at the contact points.

Since the simulation of laboratory rock tests, such as uniaxial compression test, require quasi-static loading, the coefficients of viscous contact damping are determined to provide critical viscous damping that approximates quasi-static loading. The coefficients of viscous contact damping in both normal and shear directions are given by  $C_n$  and  $C_s$ , respectively, with the

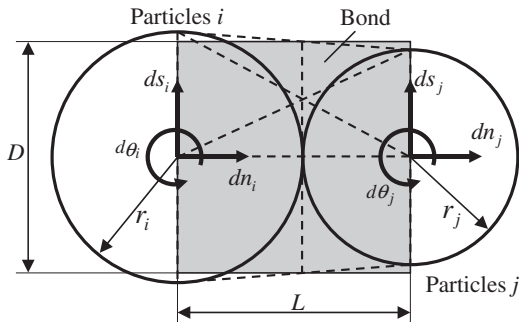


Fig. 1. Bonded particles model.

following equations:

$$C_n = 2\sqrt{m_{ij}k_n} \tag{6}$$

$$C_s = C_n\sqrt{k_s/k_n} \tag{7}$$

where  $m_{ij}$  is given by the mass of two particles  $m_i$  and  $m_j$ , as follows:

$$m_{ij} = \frac{2m_i m_j}{m_i + m_j} \tag{8}$$

If the stiffness of the springs,  $k_n$ ,  $k_s$ , and  $k_\theta$  are set as tuning parameters treated independently, a large effort will be required to determine appropriate values for them. Therefore, the stiffness of the normal and rotational springs,  $k_n$  and  $k_\theta$  are calculated using beam theory, and the stiffness of shear springs  $k_s$  is calculated by multiplying the stiffness of the normal spring  $k_n$  and a constant stiffness ratio  $\alpha$ . Thus, the stiffness of the springs given by the following equations:

$$k_n = \frac{E_p A}{L} \tag{9}$$

$$k_s = \alpha k_n \tag{10}$$

$$k_\theta = \frac{E_p I}{L} \tag{11}$$

where  $A$  is the cross-sectional area of the bond, and  $I$  is the moment of inertia of the bond.  $E_p$  is Young's modulus of particle and bonds. The moment of inertia  $I$  depends on the shape of the cross-section, and rectangular cross-section is assumed in this study.

Young's modulus  $E_p$  assigned to the particles and the stiffness ratio  $\alpha$  are microscopic parameters, and these values are different from Young's modulus and Poisson's ratio of the rocks obtained from the laboratory experiments and simulation of the uniaxial compression tests.

The normal stress  $\sigma$  and shear stress  $\tau$  acting on the cross-section of the bond are calculated using the following equations. The stress and the strain are positive in compression:

$$\sigma = \frac{f_n}{D} \tag{12}$$

$$\tau = \frac{f_s}{D} \tag{13}$$

## 2.2. Microcrack generation

When  $\sigma$  exceeds the strength of normal spring  $\sigma_c$  or  $\tau$  exceeds the strength of shear spring  $\tau_c$ , then the bond breaks and three springs are removed from the model altogether. The criteria for bond break are summarized as follows. They imply that the normal spring breaks only by tension, and compression does not cause the bond breaks.

Bond break criterion 1:  $|\sigma| \geq \sigma_c$  and  $\sigma < 0$  (tensile stress)

Bond break criterion 2:  $|\tau| \geq \tau_c$

Each bond breakage represents the generation of microcracks. A microcrack is generated at the contact point between two particles. A crack length is assumed to be the same as the bond diameter  $D$ , and the direction of it is perpendicular to the line joining the two centers.

In the parallel-bond model developed by Potyondy and Cundall [15], the moment acting on the parallel-bond (which is

expressed as elastic beam) contributes the normal stress acting on the particles. This means that the bond breakage is judged by the maximum tensile stress acting on the cross-section of the assumed elastic beam of their model. On the other hand, in this study, since the spring is introduced to restrict the rotation of the particles and used only to calculate the moment acting on the particles, the normal stress calculated by Eq. (12) does not include the moment of the elastic beam. This means that the bond breakage in the model presented here is judged by the average normal stress acting on the cross-section of the assumed elastic beam. Moreover, this procedure makes it possible to calibrate the tensile strength  $\sigma_c$  and the shear strength  $\tau_c$  almost independently. This is the difference in the mechanism of particle bondage between the parallel-bond model proposed by Potyondy and Cundall and the model presented in this research.

### 2.3. Classification of crack modes

In the AE measurement during the laboratory experiment, the AE hypocenter can be calculated from the arrival time of the P-wave first motion and the source mechanism of AE events are determined from the spatial distribution of the P-wave first motion polarities [16]. For tensile cracks, all sensors detect the P-wave first motion as compression wave. On the other hand, for shear cracks, both compressional and dilatational P-wave first motions are detected. This polarity of the P-wave first motion will depend on the stress state at the crack generation. Therefore, in this study, the crack modes can be classified using shear–tensile stress ratio  $|\tau/\sigma|$  regardless of broken spring type (normal or shear springs) as follows:

- Crack classification criterion 1:  $|\tau/\sigma| \leq 1$  and  $\sigma < 0$  (tensile stress) → tensile crack.  
 Crack classification criterion 2:  $|\tau/\sigma| > 1$  and  $\sigma < 0$  (tensile stress) → shear crack.  
 Crack classification criterion 3:  $\sigma > 0$  (compressive stress) → shear crack.

When a microcrack is generated, the strain energy stored in both normal and shear springs at the contact point is released. This produces a force imbalance, and the subsequent stress redistribution induces an AE event. The magnitude of this AE event is related to the kinetic energy generated in the model, which propagates outward from the bond breakage points.

Though the strain energy at the contact point does not equal to the magnitude of the AE event, the magnitude of AE event would strongly relate to the released strain energy. For this reason, the strain energy  $E_k$  calculated using Eq. (14) is assumed to be the energy corresponding to the magnitude of the AE event:

$$E_k = \frac{f_n^2}{2k_n} + \frac{f_s^2}{2k_s} \quad (14)$$

### 2.4. Fluid flow algorithm

The fluid flow algorithm [13,17–19] that can consider the fluid viscosity and permeability is introduced into the DEM program to reproduce the hydraulic fracturing. In the fluid flow algorithm, as shown in Fig. 2, the aperture between the adjoining particles is assumed to be a flow channel, and a series of enclosed domain is created by connecting the centers of adjoining particles.

As shown in Fig. 3, each channel is assumed to be a set of parallel plates with some aperture, and the fluid flow in the channel is modeled by the Poiseuille equation. Therefore, the volumetric

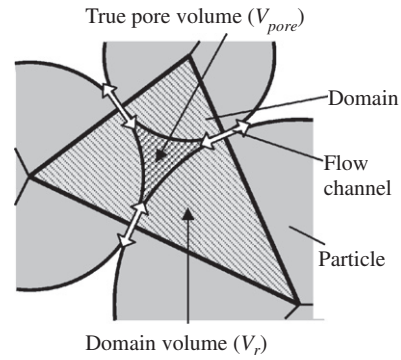


Fig. 2. Channel–domain model.

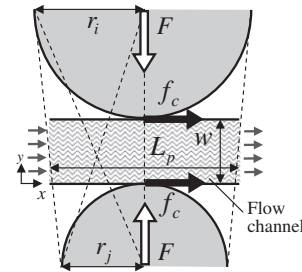


Fig. 3. Fluid flow in a channel.

laminar flow rate is given by the following equation [20]:

$$Q = \frac{w^3 \Delta P}{12\mu L_p} \quad (15)$$

where  $w$  is the aperture,  $L_p$  is the length of the channel,  $\Delta P$  is the difference in pressure across a channel, and  $\mu$  is the viscosity of the fluid. Because the model is 2D, an out of plane thickness is assumed to be a unit.  $L_p$  is assumed to be obtained from harmonic mean of the radius of two particles  $r_i$  and  $r_j$ , and given by

$$L_p = \frac{4r_i r_j}{r_i + r_j} \quad (16)$$

According to Eq. (15), fluid flow never occur when the two particles are in contact ( $w=0$ ). To avoid this, the  $w$  will be given by Eq. (17) relating to the compressive normal force  $F$  at the contact:

$$w = \frac{w_0 F_0}{F + F_0} \quad (17)$$

where  $w_0$  is assumed to be the initial aperture for particles that are just touching and  $F_0$  is the normal force at which the channel aperture decreases to half of its initial aperture. Since flow rate  $Q$  in Eq. (15) is microscopic flow rate in one flow channel and the fluid flow in a rock model is expressed by assembly of many flow channels, the permeability of the entire rock model cannot be calculated directly from Eq. (15). Therefore, the value of  $w_0$  is determined as the permeability of the entire rock model obtained by simulating the permeability test corresponds to the value of an actual specimen. This implies that the permeability of the entire rock model can be adjusted by tuning the value of  $w_0$ , and particle displacement updates the porosity and permeability of the rock model.

Each domain accumulates the fluid pressure acting on the surface of surrounding particles, and the fluid pressure is updated during the fluid flow calculation. The change of fluid pressure  $dP$

is given as the following equation by the continuity equation

$$dP = \frac{K_f}{V_r} \left( \sum Q dt - dV_r \right) \quad (18)$$

where  $\sum Q$  is total flow rate for one time step from the surrounding channels,  $dt$  is duration in one time step,  $K_f$  is the fluid bulk modulus,  $V_r$  is the apparent volume of the domain, and  $dV_r$  is the change of the volume in the domain.

2.5. Fluid flow and fluid pressure

According to the fluid flow algorithm in [13], fluid pressure of each domain is acting on particles. In addition to this, the shear stress caused by fluid flow in the channel has been newly introduced in our own cord.

The fluid flow in the channel is assumed to be the two-dimensional Poiseuille flow. Therefore, the laminar flow between two parallel plates extending in  $x$  directions, as shown schematically in Fig. 3 will now be considered. The plates are at the planes  $y=0$  and  $y=w$ , and the flow is in the  $x$ -direction, hence there is no velocity component in the  $y$ -direction. The velocity distribution  $u$  for laminar flow between parallel plates is a function of  $y$  only, and given by

$$u = \frac{w^2}{2\mu} \left[ \frac{y}{w} - \left( \frac{y}{w} \right)^2 \right] \frac{\Delta P}{L_p} \quad (19)$$

Viscous fluid flow along solid boundary will induce a shear stress on that boundary. The shear stress at a surface element parallel to a plate, at the point  $y$ , is given by

$$\tau_f = \mu \frac{du}{dy} = \left( \frac{w}{2} - y \right) \frac{\Delta P}{L_p} \quad (20)$$

In particular, the wall shear stress is given by

$$\tau_{f0} = \frac{w \Delta P}{2 L_p} \quad (21)$$

Therefore, total force acting on a plate is given by

$$f_c = L_p \tau_{f0} = \frac{w}{2} \Delta P \quad (22)$$

where  $L_p$  is the length of the channel. As shown in Fig. 3, total force  $f_c$  is given to particles as a shear force that acts on the surface of two particles that form channels.

Each domain accumulates the fluid pressure, and the fluid pressure acts on the surface of surrounding particles as shown in Fig. 4. When fluid pressure  $P$  acts on a particle whose radius is  $r$ , the total force  $f_d$  that acts on the center of a particle is given by

$$f_d = \int_{-\beta}^{\beta} P \cos \theta r d\theta \quad (23)$$

where  $\beta$  is corner half-angle of a domain.

Consequently, by introducing fluid flow algorithm, the shear stress caused by fluid flow and fluid pressure accumulated in each domain is acting on particles.

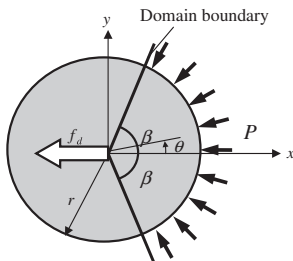


Fig. 4. Fluid pressure acting on the particle.

2.6. Saturation

Fluid flow algorithm presented in [13] assumed that the entire model is always filled with the fluid (consider only saturated condition). However, the specimen might not always be saturated in actual laboratory experiments. Such a condition with different saturation (saturated or partially saturated condition) might influence the simulation results. Therefore, to consider the partially saturated conditions, fluid flow algorithm is further improved, and the saturation factor in each domain is introduced. The saturation factor in each domain is defined as

$$S_t = \frac{V_f}{V_r \phi} \quad (24)$$

where  $V_r$  is the volume of domain as shown in Fig. 2,  $V_f$  is the volume of fluid that exists in the domain, and  $\phi$  is the assumed porosity of the model. Since the DEM model is expressed by the assembly of simple circular particles, it is difficult to reproduce the porosity of an actual rock accurately. Therefore, the assumed pore volume of the domain obtained from the entire volume of the domain,  $V_r$ , and assumed porosity,  $\phi$ , are used in Eq. (24) instead of using the true pore volume of the domain,  $V_{pore}$ .

For  $1 < S_t$  the domain is filled with fluid, while as  $1 > S_t$  the domain is partially saturated. When the partially saturated condition is considered, fluid pressure is assumed to be the same value as the atmospheric pressure (0 MPa in this research) in the partially saturated domain, and increases only after the domain is saturated.

3. Simulation condition

3.1. Rock specimen model and loading condition

Fig. 5a illustrates the rock model and loading condition for the hydraulic fracturing. The rock model is expressed by the assembly

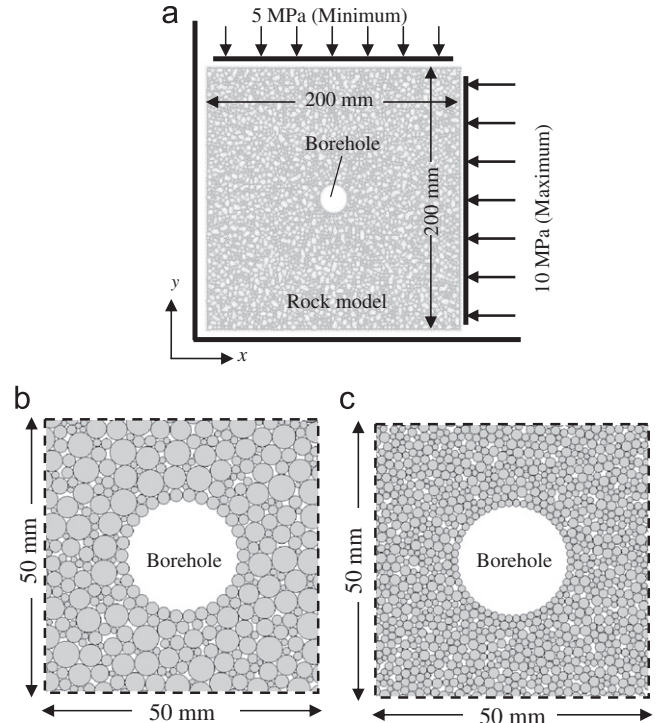


Fig. 5. Rock specimen model and loading condition: (a) rock specimen model and loading condition, (b) close-up view of model A1 (heterogeneous), and (c) close-up view of model B1 (homogeneous).

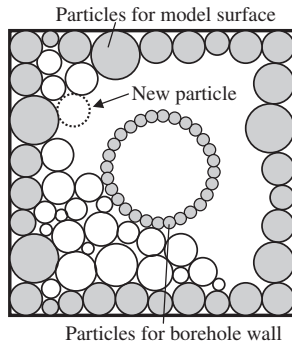


Fig. 6. Particle packing method.

of particles bonded with each other. The size of the rock specimen is 200 mm in width and 200 mm in height. A borehole for fluid injection is created at the center of the rock model. The diameter of the borehole is 20 mm. The rock model is surrounded by the four confining walls. The left and under walls are fixed and the right and upper walls can move to apply the constant confining pressure. Two confining pressures, 10 MPa in the  $x$ -direction and 5 MPa in the  $y$ -direction, were applied to the rock model. Frictional force does not applied between the model and the confining walls. The rock models used in the simulations were made according to the following procedures.

At first, particles were aligned along one edge of the model as shown in Fig. 6. The particle radius was selected following a uniform distribution between maximum and minimum radius using random number. In addition, particles that have the same radius are arranged in the circular form at the center of the model to form the inner wall of the borehole. During this process, the edge of the model and the surface of borehole can be smoothed, and unnecessary stress concentration that originates in the model geometry can be avoided. After arraying particles along the every side of the model and the inner wall of the borehole, the inside of the model is filled with particles. The new particle radius was selected following a uniform distribution between maximum and minimum radius using random number, and arranged to contact with the pre-existing particles with at least three contact points. This process is repeated until a new particle with minimum radius cannot be arranged.

In this study, two types of rock models with different ranges of particle radius were considered to investigate the influence of the particle size distribution on the hydraulic fracturing behavior. For each type, three rock models were generated, and totally six stochastic particle models were created. Models A1–A3 have the same particle size distribution with different random particle packing, and are called “heterogeneous models”. The number of particles for a heterogeneous model is about 6500 with the particle radius range from 0.5 to 2.5 mm. On the other hand, models B1–B3 are called “homogeneous models”. The number of particles for a homogeneous model is about 18,000 with the particle radius range from 0.5 to 1.0 mm. Fig. 7 shows the particle size cumulative curve for heterogeneous models and homogeneous models. Fig. 5b and c illustrates the close-up view of the heterogeneous model A1 and homogeneous model B1, respectively.

Although the microscopic parameters, such as Young’s modulus of particles and strength of the spring, are the same through a rock model, the stiffness of the bonding springs, and the stress acting on the bonds are given as a function of the particle radius by Eqs. (9)–(13). Therefore, the stress distribution in the rock model is irregularly distributed according to the distribution of the particle radius. Model A1–A3 with wide ranges of particle radius become more heterogeneous than models B1–B3. For this

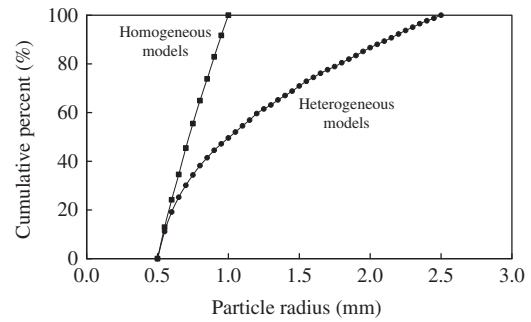


Fig. 7. Particle size cumulative curves of the heterogeneous models (models A1–A3) and the homogeneous models (models B1–B3).

reason, models A1–A3 are assumed to be heterogeneous models and models B1–B3 are assumed to be homogeneous models.

In addition, a low viscosity fluid (0.1 mPa s) and a high viscosity fluid (100 MPa s) are used as the fracturing fluid to investigate the influence of the fluid viscosity on the hydraulic fracturing behavior. Fracturing fluid was injected at constant pressurizing rate.

### 3.2. Calibration

The microscopic mechanical parameters used in this simulation were calibrated by preliminary simulations of uniaxial compression and Brazilian tests. In this study, macroscopic mechanical properties of Kurokamijima granite were used to calibrate the microscopic parameters. The confining wall is assumed to be steel. The microscopic mechanical parameters used in this simulation and the calibration results are shown in Table 1. The macroscopic parameters of both rock models show good agreement with the experimental results.

As mentioned above, since the permeability of the rock model cannot be determined directly, the value of  $w_0$  is calibrated as the permeability of the entire rock model obtained by simulating the permeability test. A rock model with 200 mm in width and 100 mm in height was used for the permeability test. At the initial condition, all domains in the rock model are fully saturated. The fluid flow was established through the model by maintaining the fluid pressure  $P_{in}$  on the left-hand side of the model at 0.2 MPa and the fluid pressure  $P_{out}$  on the right-hand side of the model at 0.1 MPa. This pressure difference causes fluid flow only through the existing network of flow channels. Fluid flow does not occur through the upper and under side of the model. The simulation of the permeability test is continued until the inflow  $Q_{in}$  equals outflow  $Q_{out}$  and a steady flow state is achieved ( $Q = Q_{in} \cong Q_{out}$ ).

Assuming the rock model as an isotropic medium and according to Darcy’s law, the steady flow rate  $Q_{steady}$  is given as

$$Q_{steady} = \frac{kH(P_{in} - P_{out})}{\mu W} \quad (25)$$

where  $\mu$  and  $k$  are the viscosity of the fluid and the macroscopic permeability of the rock model. Thus the permeability of the rock model can be given by

$$k = \frac{Q_{steady}\mu W}{H(P_{in} - P_{out})} \quad (26)$$

### 3.3. Calculation procedure for the stress distribution in DEM model

In the DEM, a particle is in contact with many others, and the contact forces, such as normal and tangential force acting on each contact point, are calculated individually. These contact forces are

**Table 1**  
Rock model properties and input parameters.

Model properties	Heterogeneous	Homogeneous
Number of particles (approximately)	6500	18,000
Maximum particle radius (mm)	2.5	1.0
Minimum particle radius (mm)	0.5	0.5
Porosity of the model (%)	12.5	18.5
Width (mm)	200	200
Height (mm)	200	200
Borehole diameter (mm)	20	20
<b>Microscopic parameters</b>		
Particle density (kg/m <sup>3</sup> )	2620	2620
Young's modulus of wall ( $E_w$ ) (GPa)	200	200
Friction coefficient of wall ( $\tan \phi_w$ )	0.0	0.0
Poisson's ratio of wall ( $\nu_w$ )	0.3	0.3
Young's modulus of particle ( $E_p$ ) (GPa)	66	84
Friction coefficient of particle ( $\tan \phi_p$ )	0.5	0.5
Poisson's ratio of particle ( $\nu_p$ )	0.25	0.25
Shear/normal spring stiffness ratio ( $\alpha$ )	0.55	0.7
Shear strength of bonding ( $\tau_c$ ) (MPa)	157.5	249
Tensile strength of bonding ( $\sigma_c$ ) (MPa)	15.8	21
Assumed porosity of the model ( $\phi$ ) (%)	0.2	0.2
Initial saturation ( $S_r$ ) (%)	10	10
Initial aperture ( $w_0$ ) (m)	$7.028 \times 10^{-7}$	$5.775 \times 10^{-7}$
Bulk modulus of the fracturing fluid ( $K_f$ ) (GPa)		2.0
Fluid viscosity for low viscous fluid ( $\mu$ ) (mPa s)		0.1
Fluid viscosity for high viscous fluid ( $\mu$ ) (mPa s)		100
<b>Calibration results</b>		
	<b>Experiment</b>	<b>Simulation</b>
	<b>Kurokamishima-granite</b>	<b>Heterogeneous      Homogeneous</b>
UCS of rock model (MPa)	200.0	199.5      199.9
Tensile strength (MPa)	10.0	10.2      10.2
Young's modulus (GPa)	70.0	70.3      70.2
Poisson's ratio	0.250	0.254      0.248
Permeability (m <sup>2</sup> )		$1.0 \times 10^{-17}$ $1.0 \times 10^{-17}$

in various directions according to the direction of contact. Therefore, to discuss the stress state in the DEM model, the contact forces acting on each contact point should be converted into the stress distribution. In this research, the stress acting on a particle is calculated by the following procedure.

As shown in Fig. 8, the normal and tangential contact force  $f_n$  and  $f_s$  are acting on a particle, and the imaginary forces  $f'_n$  and  $f'_s$  are assumed. The two sets of forces  $f'_n$  and  $f'_s$ , and  $f_n$  and  $f_s$  are of the same magnitude and opposite in direction, respectively. The normal force  $f_n$  is parallel to the  $x$ -axis. Suppose that these forces are acting on a small area as shown in Fig. 8, and are in equilibrium. The stresses that acts on the small area are given by

$$\sigma_x = \frac{f_n}{D} \tag{27}$$

$$\sigma_y = 0 \tag{28}$$

$$\tau = \frac{f_s}{D} \tag{29}$$

where  $D$  is contact width, given by Eq. (5).

Then, the normal and shear stresses,  $\sigma_x$ ,  $\sigma_y$ , and  $\tau_{xy}$  are obtained at the center of the particle, expressed with respect to the local coordinates  $xy$ . As shown in Fig. 8, the new global coordinate set  $XY$  will now be considered, and the new stresses,  $\sigma'_x$ ,  $\sigma'_y$ , and  $\tau'_{xy}$  expressed in the global coordinate set  $XY$  are given as follows [21]:

$$\sigma'_x = \frac{\sigma_x + \sigma_y}{2} + \frac{\sigma_x - \sigma_y}{2} \cos 2\theta + \tau_{xy} \sin 2\theta \tag{30}$$

$$\sigma'_y = \frac{\sigma_x + \sigma_y}{2} - \frac{\sigma_x - \sigma_y}{2} \cos 2\theta - \tau_{xy} \sin 2\theta \tag{31}$$

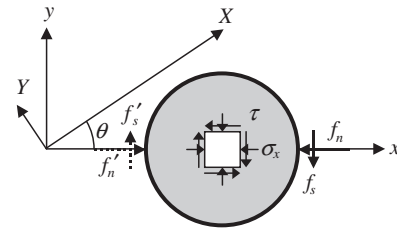


**Fig. 8.** Normal and shear stress acting on a particle.

$$\tau'_{xy} = -\frac{\sigma_x - \sigma_y}{2} \sin 2\theta + \tau_{xy} \cos 2\theta \tag{32}$$

where  $\theta$  is the rotation angle from the local coordinates  $xy$ , with counterclockwise angles taken as positive.

These calculations are applied to all contact points of one particle, and the total stresses,  $\sigma_x$ ,  $\sigma_y$ , and  $\tau_{xy}$  are obtained from the accumulation of the stress calculated by Eqs. (30)–(32) for each contact point. Since the imaginary forces  $f'_n$  and  $f'_s$  are assumed, the total stresses are divided by two. The total stresses,  $\sigma_x$ ,  $\sigma_y$ , and  $\tau_{xy}$  are given by

$$\sigma_x = \frac{\sum \sigma'_{xi}}{2} \tag{33}$$

$$\sigma_y = \frac{\sum \sigma'_{yi}}{2} \tag{34}$$

$$\tau_{xy} = \frac{\sum \tau'_{xyi}}{2} \tag{35}$$

Consequently, the stresses that act on the each particle are obtained. However, these are discrete data. To investigate the tendency and/or the character of the stress distribution in detail, the continuation of obtained discrete data (interpolation) is necessary. In this research, Inverse Distance Weighting (IDW) was used as a technique for interpolation.

IDW is one of the most commonly used techniques for interpolation, and based on the assumption that the interpolating surface is a weighted average of the discrete data and the weight assigned to each discrete data diminishes as the distance from the interpolation point to the data point increases. The simplest form of IDW is called “Shepard’s method” [22]. The equation used is as follows:

$$Z_j = \frac{\sum_{i=1}^n Z_i d_{ij}^{-m}}{\sum_{i=1}^n d_{ij}^{-m}} \quad (36)$$

where  $Z_j$  denotes an interpolated (arbitrary) value,  $Z_i$  is the discrete data ( $i=1, 2, \dots, n$ ),  $d_{ij}$  is the distance from the data point to the interpolation point,  $n$  is the total number of data points within the maximum distance from the interpolation point, and  $m$  is the positive real number, called the power parameter and controls how the weighting factors drop off as distance from the reference point increases. For  $0 < m < 1$  interpolated value  $Z_j$  has smooth peaks over the interpolated points, while as  $m > 1$  the peaks become sharp. Here, the maximum distance from the interpolation point to the data point is four times as large as maximum particle radius in DEM simulation, and the power parameter  $m=1$  is employed in this research.

#### 4. Summary of the simulation results

As mentioned in Section 3.1, the rock model A1–A3 are heterogeneous models, and the rock model B1–B3 are homogeneous models. The low viscosity fluid (0.1 mPa s) and the high viscosity fluid (100 mPa s) were used as a fracturing fluid. Thus, 12 cases of hydraulic fracturing simulations with different combination of rock model and fracturing fluid were performed. In all cases, two confining pressures, 10 MPa in the  $x$ -direction and 5 MPa in the  $y$ -direction, were applied to the rock model.

Simulation results, such as crack initiation pressure, breakdown pressure and the number of microcracks generated during the simulation, are shown in Table 2. In this paper, the case using model A1 and low viscosity fluid is called “case A1—low”, and the other cases are also named in the same manner. As shown in Table 2, when the high viscosity fluid was used, the crack

initiation pressure and the breakdown pressure becomes higher than that with low viscosity fluid regardless of the rock model.

Since the number of particles of a homogeneous model is larger than that of a heterogeneous model, the number of bonds between particles of a homogeneous model is also larger than that of a heterogeneous model. Therefore, total number of microcracks becomes large when a homogeneous model was used.

In all cases, percentage of tensile crack generation is 90% or more. The conventional theory presumes that the hydraulic fracture is created by a tensile crack that extends along the direction of maximum compressive principal stress [1]. Thus, even though a few shear cracks were generated, tensile cracks were dominant in all cases as expected in theory. However, this result is not in agreement with the result obtained from the laboratory AE measurement experiments [6]. This disagreement

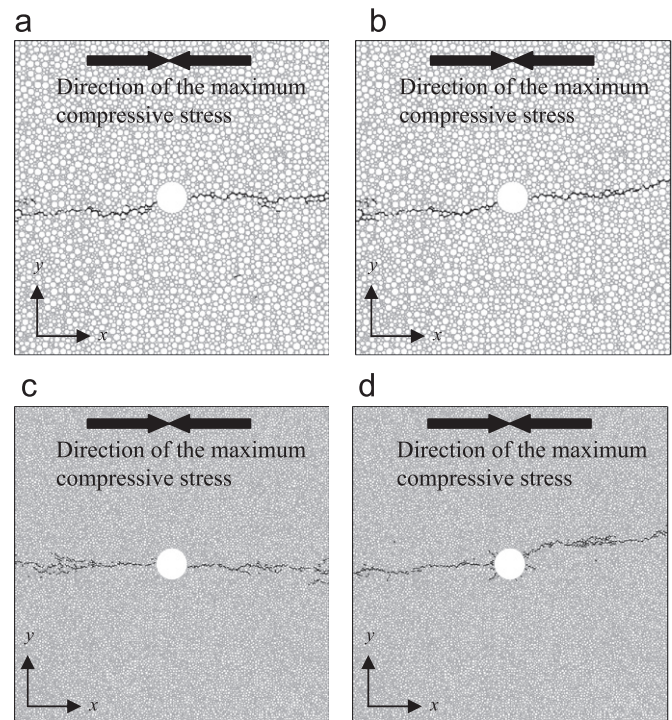


Fig. 9. Spatial distribution of all the cracks obtained from each case. The solid lines indicate the crack generations: (a) case A1—low, (b) case A1—high, (c) case B1—low, and (d) case B1—high.

Table 2  
Summary of the simulation results.

	Crack initiation pressure (MPa)	Breakdown pressure (MPa)	The number of microcracks	
			Tensile crack (%)	Shear crack (%)
Case A1—low	19.73	21.40	151 (93.8)	10 (6.2)
Case A1—high	23.84	26.09	144 (94.1)	9 (5.9)
Case A2—low	18.40	18.89	159 (94.6)	9 (5.4)
Case A2—high	21.14	37.41	260 (90.9)	26 (9.1)
Case A3—low	20.91	20.96	131 (95.6)	6 (4.4)
Case A3—high	23.39	27.20	154 (92.2)	13 (7.8)
Case B1—low	20.26	21.34	261 (98.5)	4 (1.5)
Case B1—high	23.84	40.42	258 (91.2%)	25 (8.8)
Case B2—low	20.02	22.32	236 (97.1)	7 (2.9)
Case B2—high	24.74	39.46	319 (90.9)	32 (9.1)
Case B3—low	17.32	20.21	314 (99.0%)	3 (1.0)
Case B3—high	23.79	37.95	247 (90.8)	25 (9.2)

between the simulation results and the experimental results will be discussed in Section 7.1.

In almost all cases, percentage of shear crack generation was small when the low viscosity fluid was used. This tendency is clearly shown in cases of using the homogeneous models (models B1–B3). On the other hand, when a heterogeneous model (models A1–A3) was used, influence of the fluid viscosity on the crack mode seems relatively small except for the case A2–high. The shear crack generation in case A2–high will be explained in Section 7.2.

In this study, two types of rock models and two types of fracturing fluid were used. When the combination of the type of rock model and the fracturing fluid are the same, similar results

were obtained as shown in Table 2. Therefore, case A1–low, A1–high, B1–low, and B1–high are considered to be the representative cases in this paper. Fig. 9 illustrates the geometry of the fracture formed in these cases. For all cases, the orientation of the hydraulic fractures was parallel to the direction of maximum compressive principal stress as expected in theory. This result indicates that the effect of the confining stress was appropriately expressed in the DEM simulations.

Fig. 10a–d shows the location of x-coordinates of the cracks versus time step. The crack mode is identified based on the criterion described in Section 2.3. A tensile crack is expressed with a closed circle and a shear crack is expressed with an open circle. Fig. 10e

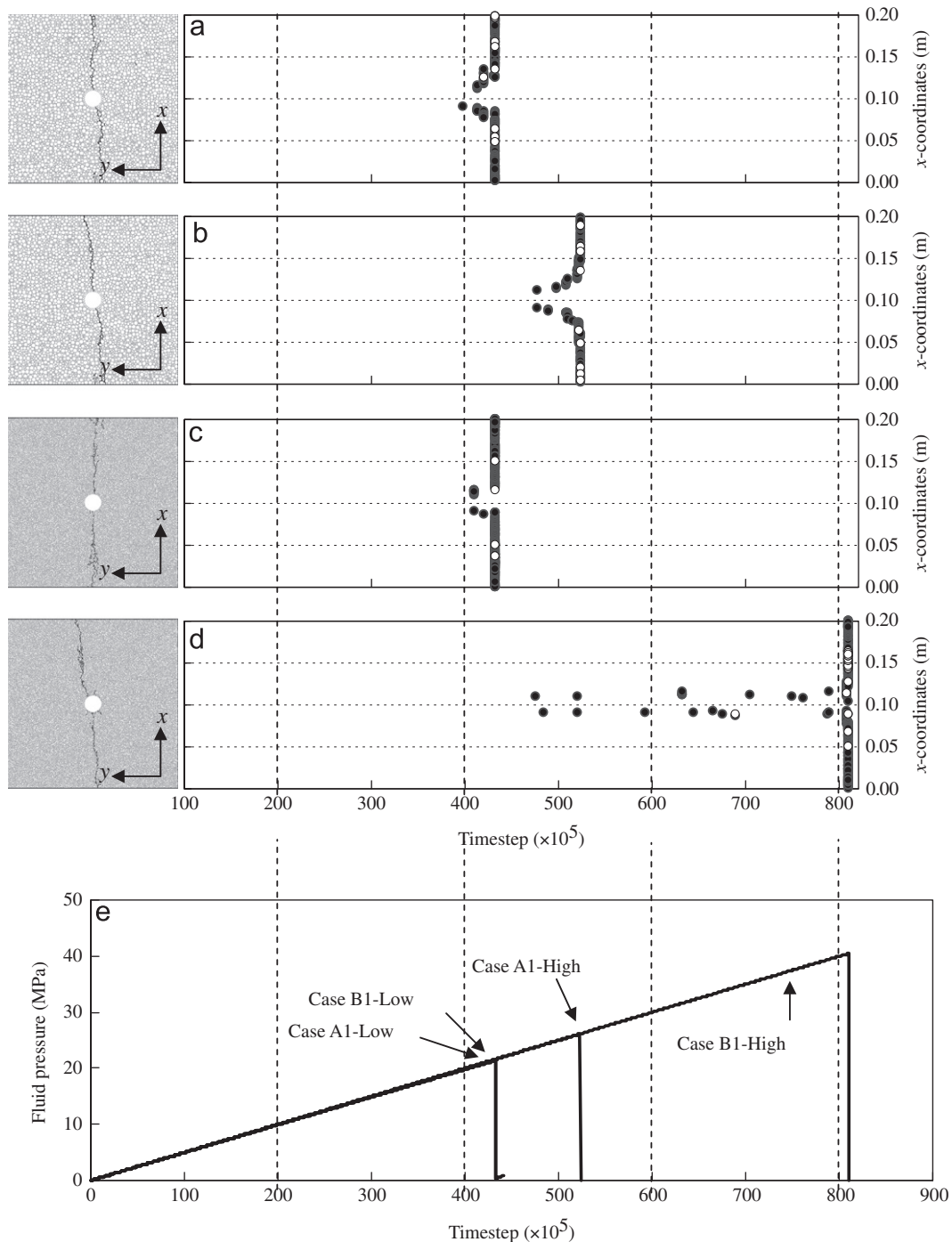


**Fig. 10.** Results of the hydraulic fracturing simulation. Time-space distribution of cracks generated in each cases: (a) case A1–low, (b) case A1–high, (c) case B1–low, (d) case B1–high, and (e) evolution of borehole pressure.

shows the evolution of the fluid pressure in the borehole. Hydraulic fracturing has been initiated before the breakdown (peak) pressure in all cases. This result agrees well with the hydraulic fracturing process deduced from AE measurements in the laboratory experiments conducted by some researchers [23,24].

### 5. Crack initiation pressure

As shown in Table 2, when the low viscosity fluid was used, the crack initiation pressure was lower than those with high viscosity fluid. For the case of using the low viscosity fluid, the crack initiation pressure was about 20 MPa. On the other hand, the crack initiation pressure was about 23 MPa for the case of using the high viscosity fluid. This result can be explained by the effect of fluid infiltration and pore pressure gradient around the borehole. There is large number of small pores inside of rocks.

When the borehole pressure increases with fluid injection, fracturing fluid penetrates into the interconnected pores of a rock from borehole wall. The fluid penetration causes an additional pore pressure around the borehole. The pore pressure reduces the effective stress of rock around the borehole, and makes it easy to generate microcracks [25].

To investigate the effect of fluid infiltration on the tensile rupture of permeable rock, Haimson [26,27] developed a sophisticated model theoretically to consider the fluid penetration. Moreover, Ito [28] and Ito and Hayashi [29] developed a new theory based on the point stress criterion. This theory assumes that the fracture initiation occurs when the maximum tensile effective stress first reaches the tensile strength of a rock at a point not on the wellbore surface but inside of the rock.

Fig. 11 shows close-up view of the rock model around the borehole for each case at the time step just before the crack initiation. The solid lines indicate the fluid penetration (saturated)

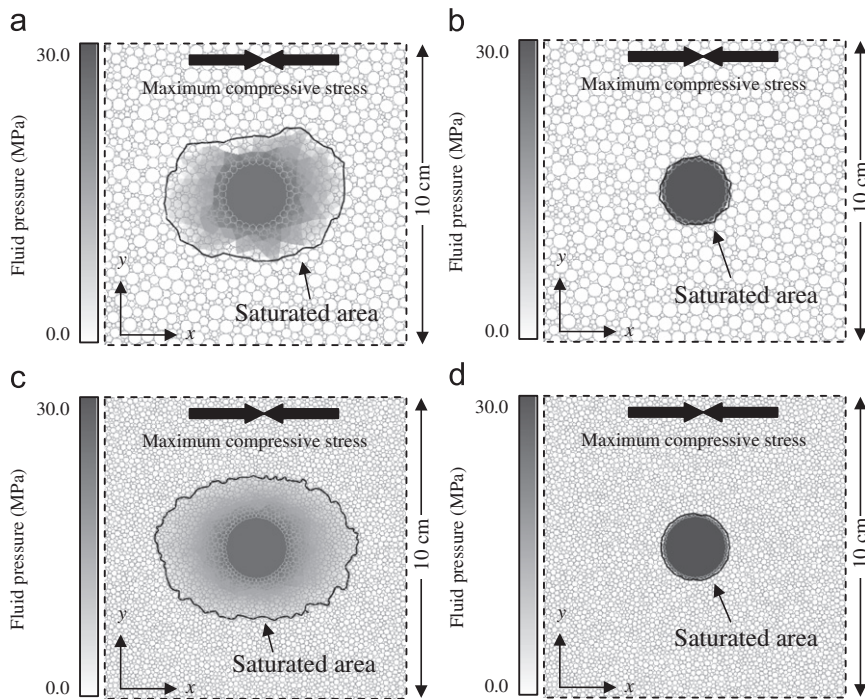


Fig. 11. Close-up view of the rock model around the borehole in each case at the time step just before the crack initiation. The solid lines indicate the fluid penetration (saturated) area and the shade of each domain indicates the fluid pressure: (a) case A1—low, (b) case A1—high, (c) case B1—low, and (d) case B1—high.

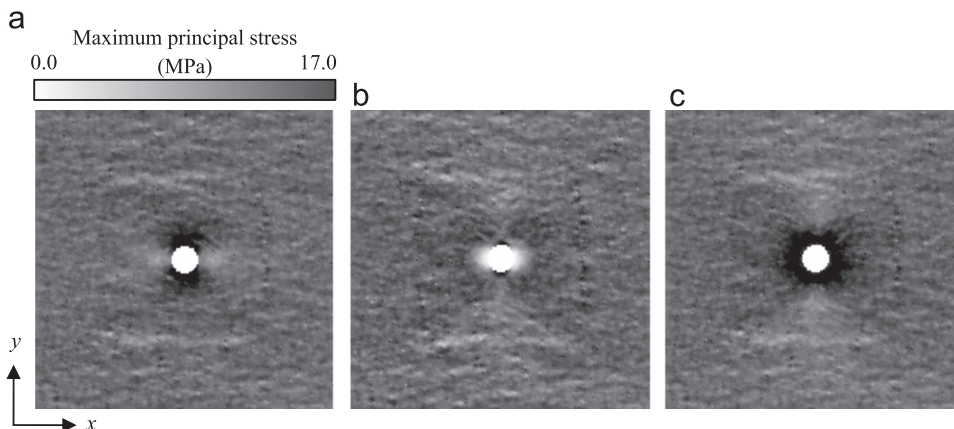


Fig. 12. Spatial distribution of magnitude of the maximum principal stress at the initial step and at the time step just before the crack initiation: (a) initial step (fluid pressure: 0 MPa); (b) case B1—low (fluid pressure: 20.26 MPa); (c) case B1—high (fluid pressure: 23.84 MPa).

area and the shade of each domain indicates the fluid pressure. As mentioned in Section 2.5, saturated area is judged by the saturation factor,  $S_r$ , calculated by Eq. (24). For  $S_r > 1$  the domain is assumed to be saturated. When low viscosity fluid was used, fracturing fluid widely infiltrated into the rock model from borehole wall and fluid pressure around the borehole increased. According to Eq. (17), the flow rate between particles is affected by the compressive normal force at the contact point. When the compressive normal force increases, the aperture of the channel,  $w$ , decreases. Therefore, since the maximum confining pressure is 10 MPa in the  $x$ -direction, fluid flow perpendicular to the  $x$ -axis decreases. Thus, the fluid saturation area is not a circle but an oval shape. On the other hand, fracturing fluid did not infiltrate into the rock model when high viscosity fluid was used.

Fig. 12a shows the spatial distribution of the maximum principal stress at the initial step. Fig. 12b and c shows the spatial distribution of the maximum principal stress in case B1—low and B1—high at the time step just before the crack initiation, respectively. The calculation procedure for the stress distribution in DEM model is described in Section 3.3. The distribution of the principal stresses is calculated based on the forces acting on the particles. In a word, Fig. 12 shows the distribution of the effective stress.

At the initial step (borehole pressure is 0 MPa), maximum principal stress exhibits mainly compressive stress in the entire model and is highest at the borehole surface across the  $y$ -axis as shown in Fig. 12a. This is in agreement with conventional elastic theory. However, as shown in Fig. 12b, the maximum principal stress around the injection hole decreased when the low viscosity fluid was used. On the other hand, when the high viscosity fluid was used, such a decrease in effective stress was not observed and maximum principal stress around the borehole increased due to the borehole pressure as shown in Fig. 12c. This result indicates

that decrease in the crack initiation pressure in case which uses low viscosity fluid is caused by decrease in effective stress due to the rise of fluid (pore) pressure around the borehole.

In actual hydraulic fracturing experiments, it is difficult to observe the infiltration behavior of fluid and change of stress distribution due to the fluid injection directly. On the contrary, the effect of fluid infiltration on the tensile rupture of permeable rock can be successfully reproduced by the coupled fluid flow and the DEM. However, several problems remain to be investigated. Schmitt and Zoback [30] discussed such the infiltration/failure problem of hydraulic fracturing in detail and suggested that the pore pressure in a low porosity specimen under rapid strain condition is diminished due to elastic pore volume expansion. This results in a higher effective confining stress near the borehole surface, and requires a higher borehole pressure at fracture initiation. This mechanism is called “dilatancy hardening” [31]. In contrast, as mentioned in Section 2.6, fluid pressure in the partially saturated domain is assumed to be 0 MPa in the simulation. Thus, dilatancy hardening explained above is not considered accurately in this study. For farther investigation into the effect of the fluid infiltration, improvement of the DEM code will be needed in the future.

## 6. Breakdown pressure

As shown in Table 2, when the high viscosity fluid was used, the breakdown pressure was markedly higher than that with low viscosity fluid. This result agrees well with the theory [23,32], and can be explained by comparison between simulation result of hydraulic fracturing by DEM and fracturing process led by Linear Elastic Fracture Mechanics (LEFM).

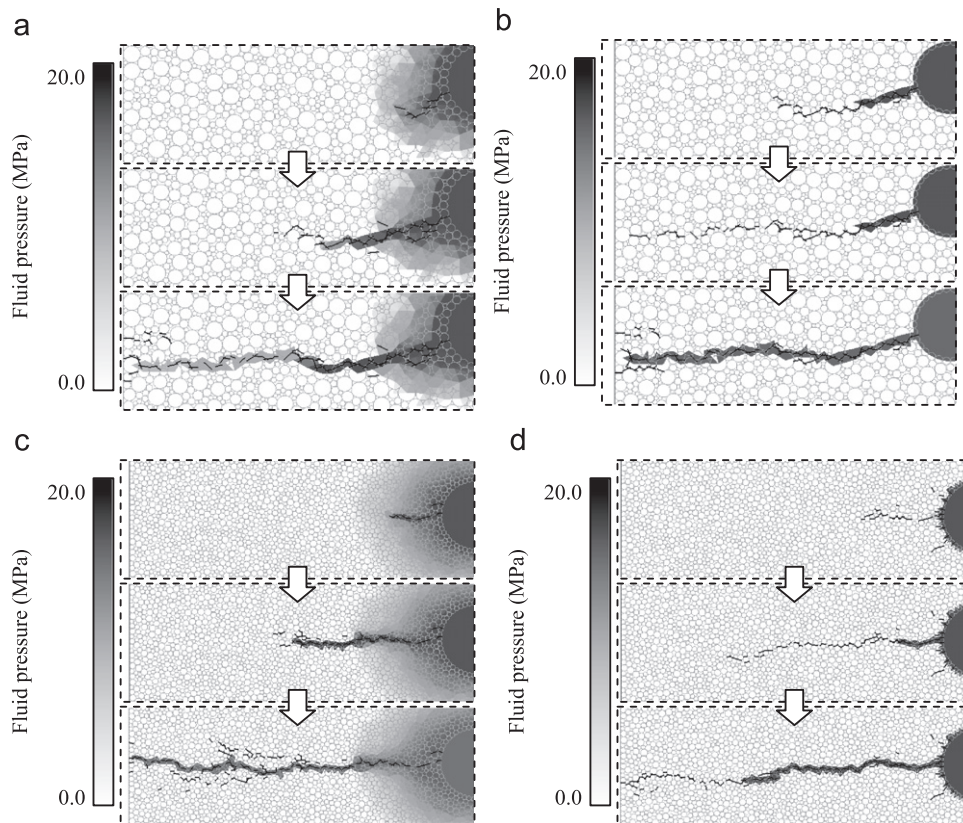


Fig. 13. Fracture propagation and fluid infiltration behavior. The solid lines indicate the crack generations and the shade of each domain indicates the fluid pressure: (a) case A1—low, (b) case A1—high, (c) case B1—low, and (d) case B1—high.

In general, LEFM is often used as an analytical technique for the propagation of the fracture in the rock like materials. LEFM is a theory that assumes application to the continuum. On the other hand, DEM is basically a discontinuity analysis technique for granular material. Therefore, the breakage of individual bonds that connect particles in DEM cannot be compared with LEFM directly. However, by assuming the connection of individual microcracks in DEM as a propagation of one macroscopic fracture, the simulation result by DEM can be interpreted by LEFM. Such a research has already been reported and it is shown that the fracture strength calculated from macroscopic fracture in DEM agree well with the one lead from LEFM [15,33,34].

Fig. 13a and b shows the fluid pressure acting on the inside of hydraulic fractures during low viscosity fluid and high viscosity fluid injection, respectively. The solid lines indicate the crack generations and the shade of each domain indicates the fluid pressure. As shown in Fig. 13a, when low viscosity fluid was used, the fluid infiltrated into the fracture immediately and the fluid pressure was applied throughout the fracture surface. On the other hand, when high viscosity fluid was used, only the fracture elongated first and then the fluid infiltrated slowly into the fracture and fluid pressure was applied only a part of the fracture surface.

Newman theoretically derived stress intensity formulae for the cases mentioned above [35]. Fig. 14 illustrates the normalized stress intensity factor at the crack tips as a function of the crack length for two cracks propagating symmetrically from a borehole in an infinite medium, and the borehole radius  $R$  is adjusted to that used in the simulation. According to Fig. 14, in case of  $\lambda=1$  (pressure acts all over the fracture surface), stress intensity factor monotonically increases with crack length. Thus, the fracture propagates continuously once it is initiated. On the other hand, in case of  $\lambda=0$  (pressure acts only in the borehole), stress intensity factor slowly decreases with crack length. Therefore, when high viscosity fluid was used as the fracturing fluid, the fracture never extends without an additional pressure. Thus, simulation result of hydraulic fracturing by DEM showed good agreement with fracturing process explained by LEFM, and the effect of fluid viscosity on the breakdown pressure was discussed.

As shown in Table 2, crack initiation pressures of heterogeneous and homogeneous model were almost the same when the same fracturing fluid was used. As mentioned in the previous section, crack initiation pressure is strongly affected by the macroscopic stress state around the borehole, and the macroscopic parameters of both rock models are the same (see Table 1). Therefore, this result seems reasonable. However, as shown in Table 2, the breakdown pressure in case of using a homogeneous model was remarkably higher than that in case of using a heterogeneous model when the high viscosity fluid was used.

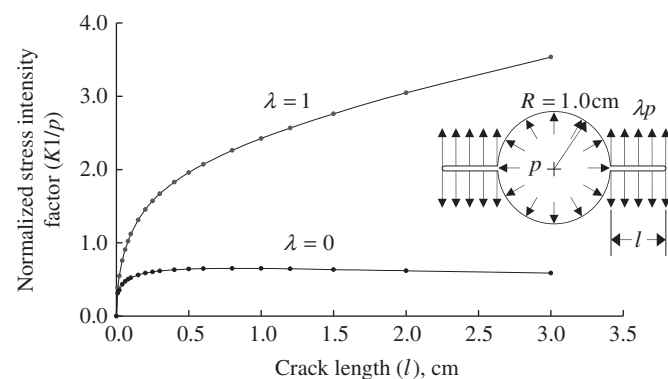


Fig. 14. Normalized stress intensity factor as a function of crack length for two radial cracks emanating from a circular hole in an infinite medium [35].

This result can be explained by the difference of crack generation processes. The propagation of fracture during hydraulic fracturing is affected by the stress intensity factor at the fracture tips as discussed above. This fact implies that the breakdown pressure is strongly affected by the microscopic properties around the fracture tip. In this study, the strength of the springs for homogeneous models is larger than those for homogeneous models although the macroscopic parameters of both rock models are the same. Moreover, the laboratory hydraulic fracturing experiment conducted by Ishida et al. [8,9] revealed that the breakdown pressure decreased with increasing grain size of the rock specimen, and they gave possible explanation for this result as follows. In an actual rock specimen, there are many pre-existing flaws such as pores, microcracks and grain boundaries, and these grain-scale discontinuities induce complex macroscopic behaviors. When rock specimen contains a lot of large grain, the flaws between the large grains become large, and the flaws would become triggers for the propagation of the fractures. Therefore, breakdown pressure decreases with increasing grain size.

For these reasons, breakdown pressure in case of using a homogeneous model became remarkably high. Meanwhile, when the low viscosity fluid is used and the fluid pressure acts all over the fracture surface, stress intensity factor monotonically increases with crack length as mentioned above. In this case, such the effect of the microscopic properties would not be essential since the fracture propagates continuously once it is initiated.

## 7. Geometry and microcracking mechanism of hydraulic fracturing

### 7.1. Hydraulic fracturing in heterogeneous model

As shown in Fig. 9a and b, the geometry of the fracture in cases A1—low and A1—high seems almost the same. However, tendency of the microcrack generation was different due to the difference of fluid viscosity. To quantify the geometry of the fracture, the total crack length and the average crack aperture are introduced. The total crack length is defined as the sum of the length of all microcracks. A crack length is assumed to be the same as the bond diameter  $D$  that given by Eq. (5). Since the model width is 200 mm and the borehole diameter is 20 mm, the total crack length becomes 180 mm when the fracture is completely straight with no branches. Thus, a large total crack length means that the geometry of the fracture is more complex. The average crack aperture is calculated at the time step when the fracturing fluid reaches the model boundary. The total crack length in A1—low and A1—high were 199 and 186 mm, respectively. On the other hand, the average crack aperture in A1—low and A1—high were 0.090 and 0.181 mm, respectively. These results indicate that the fracture in case A1—low is thin and wavelike with many secondary branches, and that the fracture in case A1—high is thick and planar fracture with few branches.

Fig. 15a and b shows the spatial distribution of all the microcracks generated during the hydraulic fracturing simulations in cases A1—low and A1—high, respectively. The closed circle indicates a location of tensile crack and the open circle indicates that of shear crack. The diameter of the circle corresponds to respective magnitude of energy obtained by Eq. (14). As shown in Fig. 15a, when the low viscosity fluid was used, the energy emitted from the shear crack was larger than that from the tensile crack. It is theoretically indicated that the energy emitted from a tensile crack is small compared with that from a shear crack [36]. The simulation results are consistent with the theory. When the low viscosity fluid was used, shear cracks emitting

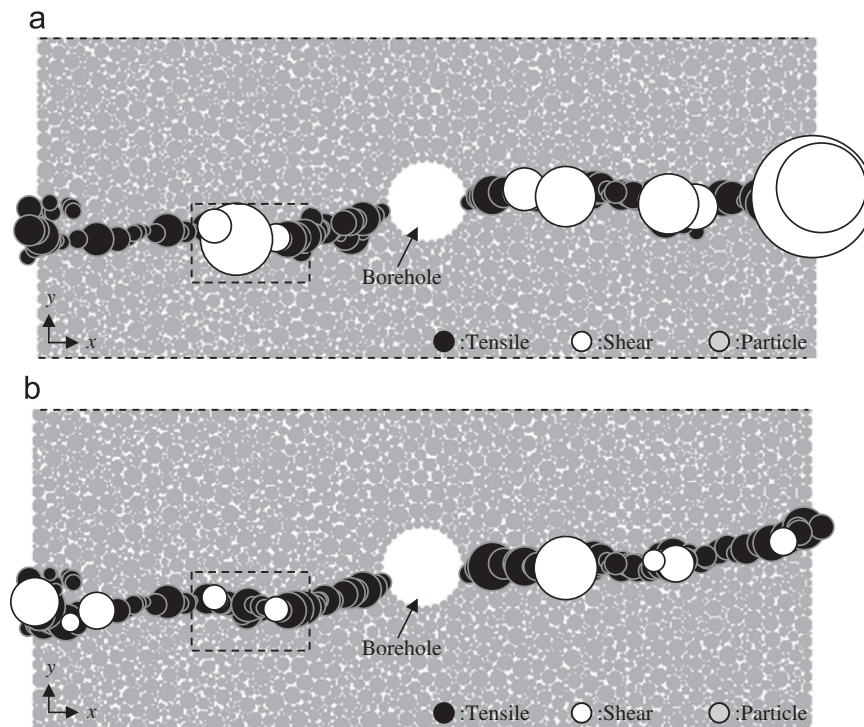


**Fig. 15.** Crack types and magnitude of energy emitted from the cracks in (a) cases A1—low and (b) A1—high (heterogeneous model). The diameter of the circle corresponds to the magnitude of crack energy.

significantly large energy were generated in the region enclosed by a dotted line square in Fig. 15a. On the other hand, when the high viscosity fluid was used, the energy emitted from the shear crack was relatively small as shown in Fig. 15b, and such a shear crack emitting large energy did not generated at the same position (see dotted line square in Fig. 15b) even though the same rock model was used. This result was caused by the difference of the fracturing process due to the difference of fluid viscosity.

Fig. 16a illustrates a close-up view of the fracture propagation and fluid infiltration behavior in case A1—low. Tensile and shear cracks are expressed as thick solid lines and open ellipses, respectively. When low viscosity fluid was used, the fracture propagated in the direction of maximum compressive stress and the fluid infiltrated into the fracture immediately. At this time, fracture was mainly formed by tensile failure, and the number of shear cracks was a few. However, when a large particle existed on the course of the fracture growth, propagation of the fracture was obstructed and the fluid pressure was applied throughout the fracture surface. Beyond the obstructing particle, tensile cracks were generated in front of the fracture tip due to the fluid pressure acting on the fracture surface because the tensile strength of bond was obviously small compared with the shear strength. Finally, when the fluid pressure acting on the fracture tip sufficiently increased, shear cracks emitting significantly large energy were formed to connect these tensile cracks. This fracturing process is similar to Hill's model, originally proposed for volcanic earthquake swarms [37].

On the other hand, Fig. 16b illustrates a close-up view of the fracture propagation and fluid infiltration behavior in case A1—high. When high viscosity fluid was used, only the fracture propagated first. At this time, microcrack geometry was similar to that in case A1—low. However, fracturing fluid did not infiltrate into the fracture immediately because the fluid viscosity was high. The fluid pressure was applied the borehole and only a part of the fracture surface. As mentioned in Section 3.1, the microscopic parameters

given to the bonds between particles, such as Young's modulus of particles and strength of the spring, are constant in this research. However, since the stiffness of the bonding springs and the stress acting on the bonds are given as a function of the particle radius by Eqs. (9)–(13), the strain energy given by Eq. (14) becomes the function of the particle radius. Hence, magnitude of the energy emitted along with microcrack generation was irregularly distributed according to the distribution of the particle radius of the rock model. The microcracks are likely to be generated between small particles and the energy emitted from such microcracks become small.

As borehole pressure increases, a number of microcracks were generated between small particles without infiltration of the high viscosity fluid. In this case, the number of shear cracks depends on the particle arrangement because the shear cracks are generated along the grain boundaries that diagonally across the direction of maximum confining stress. When these microcracks were connected and one straight fracture was formed, fracture width gradually increased due to the borehole pressure. Finally, high viscosity fluid infiltrate into the existing fracture when the fracture width sufficiently increased. As a result, the fracture became thick planar with few branches when high viscosity fluid was used, and the shear crack emitting large energy observed in case A1—low was not generated in case A1—high.

According to the microscopic observation in laboratory experiments [6,7], hydraulic fracture mainly located at the grain boundary. They also pointed out that the fracture induced by high viscosity oil injection could be observed very clearly because of their large widths, whereas fracture induced by low viscosity water injection could only be detected after careful and close observation because they were extremely thin. In addition, high viscosity oil tends to generate thick planar fracture with few branches, while low viscosity water tends to generate thin and wavelike cracks with many secondary branches. By considering the particles in DEM as the mineral grains, the fracture propagation process in the DEM simulations mentioned above gave the

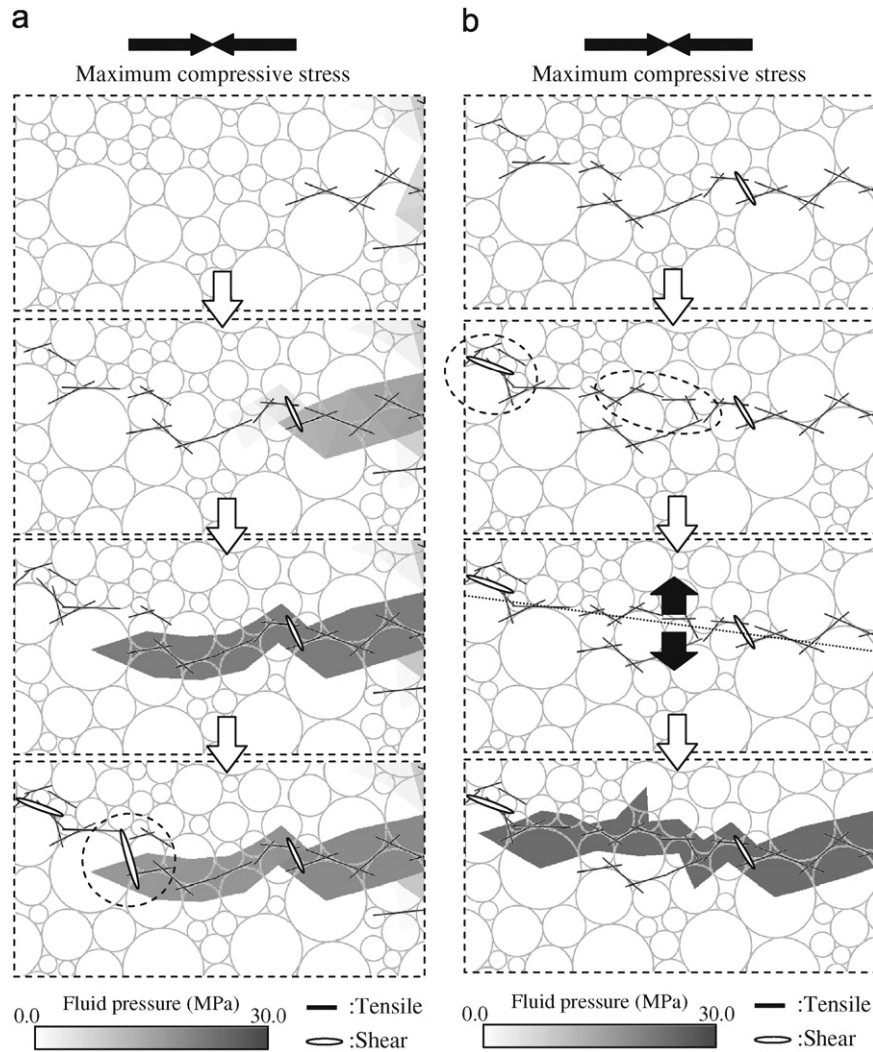


Fig. 16. Close-up view of the fracture propagation and fluid infiltration behavior: (a) case A1—low and (b) case A1—high.

rational explanation for the hydraulic fracturing behavior observed in the experiment.

As shown in Table 2, tensile cracks were dominant in all cases though a few shear cracks were generated. This result is not in agreement with the result obtained from the laboratory AE measurement experiments conducted by Ishida et al. [6]. Recorded AE waveforms in their hydraulic fracturing experiment indicated that the shear type fracturing seemed to be dominant in low viscosity water injection and both tensile and shear AE were recorded in high viscosity oil injection. This disagreement between the results obtained from the simulation and experiment can be explained by considering the energy of microcracks.

As mentioned above, when low viscosity fluid is used as the fracturing fluid, low viscosity fluid can easily infiltrate into the pores, defects and microcracks, and the hydraulic fracture has tortuous paths according to the boundary of the mineral grain. When the fluid pressure acting on the fracture tip increase sufficiently, shear cracks that emit large energy are formed to connect pre-existing microcracks. Since the tensile strength of rock is obviously small compared with the compressive strength, the energy emitted from a tensile crack is small compared with that from a shear crack. Such a small AE is easily buried in a noise and difficult to be measured in the experiments. In fact, only a few percent of the located AE events showed clearly the first motions

of the P-wave and were possible to obtain reliable mechanism solutions during hydraulic fracturing conducted by Ishida et al. even though several hundreds of AE sources were located. Hence, only for about five events in each specimen, their fracturing mechanisms could be examined based on the polarities of P-wave first motions [6,10]. Therefore, when low viscosity fluid was used, the shear type AE with large energy was dominantly observed in AE measurement experiments conducted by Ishida et al. [6].

On the other hand, when the high viscosity fluid is used, fracturing fluid cannot infiltrate into the microcracks, and one straight fracture is formed according to the stress state in the rock due to the increase in the borehole pressure. The fracturing fluid will infiltrate along existing straight fracture after enough opening of the fracture due to the borehole pressure. Although a few shear cracks are generated along the grain boundaries that diagonally across the direction of maximum confining stress, the energy emitted from these shear cracks are small as shown in Fig. 15b because such microcracks are likely to be generated between small particles. Therefore, very few shear cracks emitting large energy are observed when the high viscosity fluid is used. In addition, when the high viscosity fluid infiltrates into the fracture, fluid pressure becomes very high. Thus, in an actual hydraulic fracturing, highly pressurized fluid causes large fracture opening, and tensile AE with large energy may be generated. As a result,

both tensile and shear AE were observed during the injection of high viscosity fluid in an AE monitoring conducted by Ishida et al. [6].

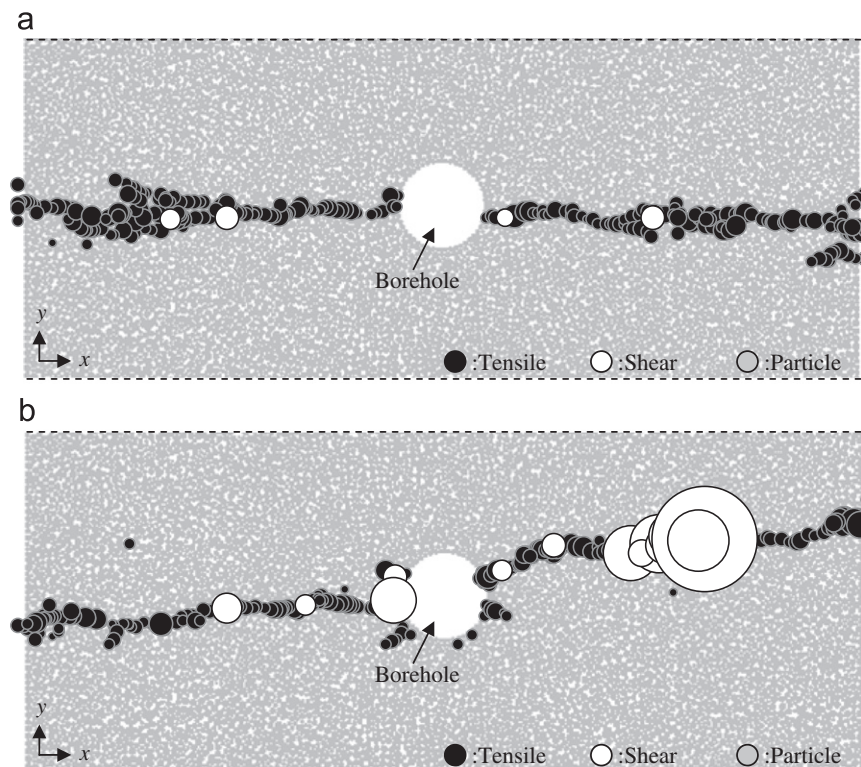
## 7.2. Hydraulic fracturing in homogeneous model

Fig. 17b shows the spatial distribution of all the microcracks and magnitude of energy in case B1—low and B1—high, respectively. By comparing Fig. 15 with Fig. 17, it is found that the energy emitted from the microcrack generation in model B1 was relatively small compared with that in model A1. This tendency agrees well with the results of the uniaxial experiments conducted by Eberhardt et al. [38] and the results of laboratory hydraulic fracturing experiment conducted by Ishida [10]. Their experimental results showed that the number of detected AE events decreased markedly with decreasing grain size. As mentioned in Section 7.1, the energy emitted along with microcrack generation is irregularly distributed according to the distribution of the particle radius of the rock model. The energy emitted from a microcrack generated between small particles becomes small. For this reason, the energy emitted from the microcrack generation in homogeneous models consisting of small particles was relatively small compared with that in heterogeneous models including many large particles.

Since the fracture path in case B1—low and B1—high was obviously different as shown in Fig. 9c and d, the geometry of the fracture could not be compared simply by the total crack length and the average crack aperture. However, Fig. 17a clearly shows that many small branching cracks were generated when the low viscosity fluid was used. On the other hand, as shown in Fig. 17b, such a branching crack was not generated when the high viscosity fluid was used. This result supports the consideration related to the influence of the viscosity of the fracturing fluid discussed in the previous section.

As shown in Table 2, percentage of shear crack generation was very small when a homogeneous model and the low viscosity fluid were used (case B1—low, B2—low, and B3—low). This tendency agrees with the experimental results. The fault plane solutions of AE implied shear type fracturing in the specimens with large grain, while they implied tensile fracturing in the specimen with small grain [7,10]. In addition, in hydraulic fracturing in an acrylic resin block, all recorded AE events indicated tensile fracturing mechanisms [7]. The acrylic resin is impermeable and could be considered to be an extremely homogeneous material. These results clearly indicate that, with decreasing grain size, the dominant micro-fracturing mechanism becomes tensile rather than shear. This result can be explained by particle size distribution of the model. As mentioned in the previous section, when the particle radius is widely distributed and relatively large particles are contained in the rock model, shear cracks generated along the grain boundaries that diagonally across the direction of maximum confining stress. On the other hand, when all particles in the rock model are small, the hydraulic fracture can develop straight in the direction of the maximum confining stress. Therefore, the number of shear cracks is very small and shear cracks that emit substantial energy are difficult to be generated in homogeneous rock model as shown in Fig. 17a.

However, as shown in Fig. 17b, when high viscosity fluid was used, many shear cracks that emit large energy were generated even in the homogeneous model. Fig. 18 shows a close-up view of the time-space distribution of cracks generated in case B1—high from time step 807–811 ( $\times 10^5$ ). This figure indicates that the fracture did not develop smoothly but developed stepwise, and such stepwise development of the fracture was lead by the generation of shear cracks. However, the number of shear cracks generated during the fracture propagation was very few, and the energy emitted from such a shear crack was small. As indicated in the region enclosed with dotted circle in Fig. 18, many shear



**Fig. 17.** Crack types and magnitude of energy emitted from the cracks in cases B1—low and B1—high (homogeneous model). The diameter of the circle corresponds to the magnitude of crack energy: (a) case B1—low and (b) case B1—high.

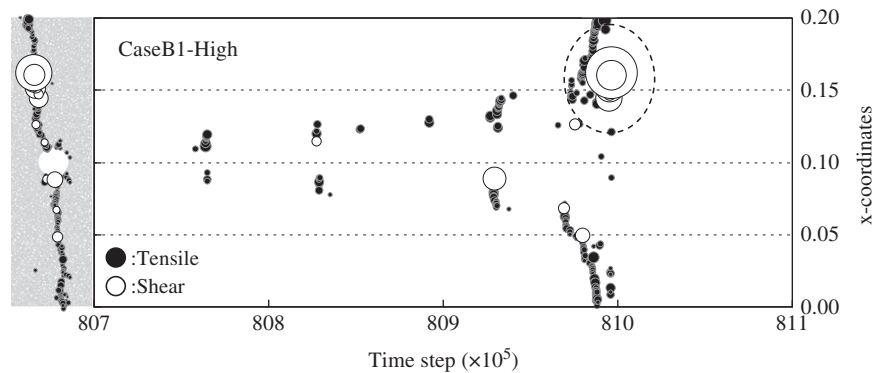


Fig. 18. Time–space distribution of cracks generated in case B1—high. Close-up view of the time steps 807–811 ( $\times 105$ ).

cracks that emit significantly large energy were generated when the fluid infiltrated into the fracture after the fracture development.

As mentioned above, shear cracks are difficult to be generated in the homogeneous model. However, the rock model is not perfectly homogeneous even when all particles in the rock model are very small because the rock model is expressed by the assembly of particles. The hydraulic fracture is microscopically tortuous due to the particle arrangement, and a few shear cracks are generated when the fracture grows diagonally across the direction of maximum confining stress. At this time, the higher fluid pressure is required to extend the fracture because a part of the confining stress and the borehole pressure act on the fracture tip as the shear stress. Thus, the fracture develops stepwise accompanied with the shear crack generation. In the actual AE measurement during hydraulic fracturing using low viscosity water and high viscosity oil injection, AE events spread from the borehole throughout the specimen, within short periods corresponding to the respective pressure drops. In particular, when the fracturing fluid was not allowed to penetrate the fracture, AE sources spread stepwise [6]. The DEM simulation results are well in agreement with these AE behaviors.

When the fracture was microscopically tortuous and there existed the region where fracture width was narrowed locally, the higher fluid pressure was required in order that a high viscosity fluid went through such a narrow region. As a result, breakdown pressure became remarkably high and many new microcracks including the shear crack were generated due to the impact of fluid infiltration as shown in the dotted circle in Fig. 18. Such large shear cracks were not seen in case A1—high and A3—high though the highly viscosity fluid was used. Since the particle number of heterogeneous models was about 1/3 of the particle numbers of homogeneous models, the region where fracture width was narrowed partially as mentioned above did not appear in these cases. However, the phenomenon similar to case B1—high possibly occurs in case of using the heterogeneous model with different particle arrangement as in the case A2—high. These shear cracks emit significantly large energy, and AE that occurs from such large shear cracks would be observed even in field scale AE measurement as reported by Baria and Green [2] and Talebi and Cornet [3]. To validate this phenomenon, more detailed analysis, such as field scale simulations, would be required.

## 8. Conclusion

A series of simulations for hydraulic fracturing in hard rock were performed by using the flow-coupled DEM code to discuss the influence of the fluid viscosity and the particle size distribution.

The simulation results show good agreement with the actual experimental results including the AE measurement data.

In this study, 12 cases of hydraulic fracturing simulations with different combination of rock model and fracturing fluid were performed. For all cases, the orientation of hydraulic fractures is parallel to the direction of maximum compressive principal stress. This result indicates that the effect of the confining stress was appropriately expressed in the DEM simulations.

Crack initiation pressure and breakdown pressure for the low viscosity fluid were lower than those for high viscosity fluid. Fracturing fluid easily penetrates through the interconnected pores into a rock from borehole wall, and the fluid penetration causes pore pressure increase around the borehole. Such an increase in pore pressure reduces the effective stress around the borehole, and induces microcracking. Thus, the crack initiation pressure with the low viscosity fluid was lower than that with high viscosity fluid.

The low viscosity fluid can easily infiltrate into the fracture and the fluid pressure was applied throughout the fracture surface. Hence, the fracture propagates continuously once it is initiated because the stress intensity factor at the fracture tip monotonically increases with crack length. On the other hand, when the high viscosity fluid is used, fluid pressure was applied only a part of the fracture surface. Therefore, the fracture never extends without an additional pressure. For this reason, when the high viscosity fluid was used, breakdown pressure was markedly higher than that with low viscosity fluid.

When the fluid pressure acting on the fracture tip increases sufficiently, shear cracks that emit large energy are formed to connect pre-existing microcracks, and the hydraulic fracture has tortuous paths according to the boundary of the mineral grain. The energy released from a tensile crack becomes small because the tensile strength of rock is obviously small. A small AE is easily buried in a noise and difficult to be measured in an experiment. Therefore, in AE measurement experiments, shear type of AE with large energy is dominantly observed though the tensile cracks are dominantly generated in the simulation. On the other hand, when the high viscosity fluid was used, the fracturing fluid will infiltrate along existing straight fracture after enough opening of the fracture due to the borehole pressure. Thus, thick and planar fracture with few branches was generated, and very few shear cracks emitting large energy were observed. As a result, both tensile and shear AE can be observed during the injection of high viscosity fluid in an actual AE monitoring.

When the particle radius is widely distributed and relatively large particles are contained in the rock model, shear cracks generated along the grain boundaries that diagonally across the direction of maximum confining stress. On the other hand, when all particles in the rock model are small, the hydraulic fracture can develop straight in the direction of the maximum confining stress.

Therefore, the number of shear cracks is very small and shear cracks which emit large energy are difficult to be generated in homogeneous rock model.

In actual hydraulic fracturing experiments, it is difficult to observe the infiltration behavior of fluid and change of stress distribution due to the fluid injection directly. On the contrary, the DEM can directly represent grain-scale microstructural features of rock, such as pre-existing flaws, pores, microcracks and grain boundaries by considering each grain as a DEM particle without complicated constitutive laws. The hydraulic fracturing process and the effect of fluid infiltration on the tensile rupture of permeable rock can be successfully reproduced and discussed in detail by the coupled fluid flow and the DEM. This suggests that the DEM model may be a strong tool to understand the fracture behavior of permeable rock.

## References

- [1] Hubbert MK, Willis DG. Mechanics of hydraulic fracturing. *Trans AIME* 1957;210:153–66.
- [2] Baria R, Green ASP. Seismicity induced during a viscous stimulation at the Camborne School of Mines Hot Dry Rock geothermal project in Cornwall, England. In: *Progress in acoustic emission III*, 1986. p. 407–29.
- [3] Talebi S, Cornet FH. Analysis of the microseismicity induced by a fluid injection in a granitic rock mass. *Geophys Res Lett* 1987;14:227–30.
- [4] Falls SD, Young RP, Carlson SR, Chow T. Ultrasonic tomography and acoustic emission in hydraulically fractured Lac du Bonnet grey granite. *J Geophys Res* 1992;97:6867–84.
- [5] Urbancic TI, Shumila V, Rutledge JT, Zinno RJ. Determining hydraulic fracture behavior using microseismicity. In: *Proceedings of the 37th US rock mechanics symposium*, 1999. p. 991–7.
- [6] Ishida T, Chen Q, Mizuta Y, Roegiers JC. Influence of fluid viscosity on the hydraulic fracturing mechanism. *J Energy Resour Technol* 2004;126:190–200.
- [7] Matsunaga I, Kobayashi H, Sasaki S, Ishida T. Studying hydraulic fracturing mechanism by laboratory experiments with acoustic emission monitoring. *Int J Rock Mech Min Sci Geomech Abstr* 1993;30:909–12.
- [8] Ishida T, Mizuta Y, Matsunaga I, Sasaki S, Chen Q. Effect of grain size in granitic rock on crack extension in hydraulic fracturing. In: *Proceedings of the fourth North American rock mechanics symposium*, 2000. p. 1105–11.
- [9] Ishida T, Sasaki S, Matsunaga I, Chen Q, Mizuta Y. Effect of grain size in granitic rocks on hydraulic fracturing mechanism. In: *Trends in rock mechanics*, Geotechnical Special Publications, vol. 102, 2000. p. 128–39.
- [10] Ishida T. Acoustic emission monitoring of hydraulic fracturing in laboratory and field. *Constr Build Mater* 2001;15:283–95.
- [11] Shah KR, Carter BJ, Ingraffea AR. Hydraulic fracturing simulation in a parallel computing environment. *Int J Rock Mech Min Sci* 1997;34:282.
- [12] Vandamme L, Curran JH. A three dimensional hydraulic fracturing simulator. *Int J Numer Methods Eng* 1989;28:909–27.
- [13] Al-Busaidi A, Hazzard JF, Young RP. Distinct element modeling of hydraulically fractured Lac du Bonnet granite. *J Geophys Res* 2005;110:B06302.
- [14] Cundall PA, Strack ODL. A discrete numerical model for granular assemblies. *Geotechnique* 1979;29:47–65.
- [15] Potyondy DO, Cundall PA. A bonded-particle model for rock. *Int J Rock Mech Min Sci* 2004;41:1329–64.
- [16] Kasahara K. *Earthquake mechanics*. Cambridge: Cambridge University Press; 1981.
- [17] Kiyama H, Nishimura T, Fujimura H. An advanced distinct element model coupling with pore water. *J Geotech Eng* 1994;499:31–9.
- [18] Bruno MS. Micromechanics of stress-induced permeability anisotropy and damage in sedimentary rock. *Mech Mater* 1994;18:31–48.
- [19] Thallak S, Rothenburg L, Dusseault M. Simulation of multiple hydraulic fractures in a discrete element system. In: *Proceedings of the 32nd US rock mechanics symposium*, 1991. p. 271–80.
- [20] Zimmerman RW, Bodvarsson GS. Hydraulic conductivity of rock fractures. *Transp Porous Media* 1996;23:1–30.
- [21] Jaeger JC, Cook NGW, Zimmerman RW. *Fundamentals of rock mechanics*. 4th ed. Oxford: Wiley-Blackwell; 2007.
- [22] Shepard D. A two-dimensional interpolation function for irregularly-spaced data. In: *Proceedings of the 1968 ACM national conference*, 1968. p. 517–24.
- [23] Zoback MD, Rummel F, Jung R, Raleigh CB. Laboratory hydraulic fracturing experiments in intact and pre-fractured rock. *Int J Rock Mech Min Sci Geomech Abstr* 1977;14:49–58.
- [24] Zhao Z, Kim H, Haimson B. Hydraulic fracturing initiation in granite. In: *Proceedings of the second North American rock mechanics symposium*, 1996. p. 1231–5.
- [25] Schmitt DR, Zoback MD. Infiltration effects in the tensile rupture of thin walled cylinders of glass and granite: implications for the hydraulic fracturing breakdown equation. *Int J Rock Mech Min Sci* 1993;30:289–303.
- [26] Haimson BC. Hydraulic fracturing in porous and nonporous rock and its potential for determining in-situ stresses at great depth. PhD thesis, University of Minnesota, Minneapolis, 1968.
- [27] Haimson BC, Fairhurst C. Initiation and extension of hydraulic fracture in rocks. *Soc Petrol Eng J* 1967;310–8.
- [28] Ito T. Effect of pore pressure gradient on fracture initiation in fluid saturated porous media. *Eng Fract Mech* 2008;75:1753–62.
- [29] Ito T, Hayashi K. Physical background to the breakdown pressure in hydraulic fracturing tectonic stress measurements. *Int J Rock Mech Min Sci* 1991;28:285–93.
- [30] Schmitt DR, Zoback MD. Diminished pore pressure in low porosity crystalline rock under tensional failure: apparent elastic dilatant strengthening. *J Geophys Res* 1992;97:273–88.
- [31] Brace WF, Martin III RJ. A test of the law of effective stress for crystalline rocks of low porosity. *Int J Rock Mech Min Sci Geomech Abstr* 1968;5:415–26.
- [32] Zoback MD, Pollard DD. Hydraulic fracture propagation and the interpretation of pressure time records for in-situ stress determination. In: *Proceedings of the 19th US rock mechanics symposium*, 1978. p. 14–22.
- [33] Huang H. Discrete element modeling of tool-rock interaction. PhD thesis, University of Minnesota, Minneapolis, 1999.
- [34] Moon T, Nakagawa M, Berger J. Measurement of fracture toughness using the distinct element method. *Int J Rock Mech Min Sci* 2007;44:449–56.
- [35] Newman JC. An improved method of collocation for the stress analysis of cracked plates with various shaped boundaries. *NASA Tech Note* 1971: D-6373.
- [36] Hayashi K, Motegi S. Characteristics of energy of elastic waves due to sudden growth of subsurface reservoir cracks for geothermal heat extraction. In: *Progress in acoustic emission*, vol. IV, 1988. p. 265–72.
- [37] Hill D. A model for earthquake swarms. *J Geophys Res* 1977;82:1347–52.
- [38] Eberhardt E, Stimpson B, Stead D. Effect of grain size on the initiation and propagation thresholds of stress-induced brittle fractures. *Rock Mech Rock Eng* 1999;32:81–99.